Particuology 11 (2013) 581–587

Contents lists available at SciVerse ScienceDirect

Particuology

journal homepage: www.elsevier.com/locate/partic

Morphology and optical absorption of $Bi_2Fe_4O_9$ crystals via mineralizer-assisted hydrothermal synthesis

Yi Liu, Ruzhong Zuo*

Institute of Electro Ceramics & Devices, School of Materials Science and Engineering, Hefei University of Technology, Hefei 230009, China

ARTICLE INFO

Article history:
Received 15 August 2012
Received in revised form 15 October 2012
Accepted 6 November 2012

Keywords:
Hydrothermal synthesis
Crystal growth
$Bi_2Fe_4O_9$ crystals

ABSTRACT

Submicron-sized $Bi_2Fe_4O_9$ crystals were successfully synthesized via the hydrothermal method, while micron-sized $Bi_2Fe_4O_9$ crystals with rod-like morphologies were obtained in the presence of the mineralizer KNO_3. X-ray diffraction, scanning electron microscopy and transmission electron microscopy were employed to characterize the products. According to a series of time-dependent experiments, it was concluded that the likeliest formation mechanism for the microrods was the Ostwald ripening process. It was proposed that the blocking effect of NO_3^- contributed to the formation of the rod-like powders. Moreover, the optical absorption of the prepared $Bi_2Fe_4O_9$ crystals was measured using an UV–vis spectrophotometer, indicating that $Bi_2Fe_4O_9$ powders can be used as effective photocatalysts under visible light.

1. Introduction

Ternary bismuth ferrites have received considerable interest in the past few years because of their potential applications in sensing, actuation, and digital memory (Valant & Suvorov, 2002; Voll, Beran, & Schneider, 2006; Wang et al., 2003). As a typical bismuth ferrite, $Bi_2Fe_4O_9$ has an orthorhombic structure (space group Pbam), with lattice constants of $a = 7.965$ Å, $b = 8.440$ Å, and $c = 5.994$ Å. Bulk $Bi_2Fe_4O_9$ ceramics display ferroelectric hysteresis loops at $T = 250$ K and antiferromagnetic ordering ($T_N = 260$ K), indicating that $Bi_2Fe_4O_9$ is a promising multiferroic material (Singh et al., 2008). Moreover, $Bi_2Fe_4O_9$ is well known as an important material for semiconductor gas sensors, owing to its high sensitivity to ethanol and acetone vapors (Poghossian, Abovian, Avakian, Mkrtchian, & Haroutunian, 1991). Because $Bi_2Fe_4O_9$ features a small bandgap near the range of visible and UV light and possesses the ability to photodegrade methyl orange (MO) (Ruan & Zhang, 2009), phenol, and aqueous ammonia (Sun, Wang, Zhang, & Shang, 2009), it is also known to be an important photocatalyst. In particular, the catalytic potential of $Bi_2Fe_4O_9$ particles, particularly for the oxidation of ammonia to NO, is of current interest because it is likely to replace the high-cost, irrecoverable, and costly catalysts (often made from platinum, rhodium, or palladium) currently used for the industrial manufacturing of nitric acid (Zakharchenko, 2002).

It is known that the properties of inorganic nanomaterials, especially the adsorption, catalytic and optical properties, not only depend on their chemical composition and phase structure but are also related to their size and morphology (Li, Lin, Zhang, Wang, & Nan, 2010; Ruan & Zhang, 2009; Zhang, Lv, et al., 2011). For example, bismuth ferrite and titania, with different morphologies, exhibit different photocatalytic properties (Fei et al., 2011; Yang et al., 2008). For the sake of morphology control, various techniques have been employed to synthesize $Bi_2Fe_4O_9$ nanostructures, including the sol–gel method (Yang, Huang, Dong, Li, & Shi, 2006; Zhang, Yang, et al., 2011), molten salt technique (Park, Papaefthymiou, Moodenbaugh, Mao, & Wong, 2005), and hydrothermal synthesis (Du, Cheng, Dou, & Wang, 2011; Han, Huang, Jia, et al., 2006; Ruan & Zhang, 2009; Sun et al., 2009; Wang et al., 2010, 2009; Xiong, Wu, Peng, Jiang, & Chen, 2004; Yu, Miao, & Tan, 2008; Zhang, Bourgeois, Yao, Wang, & Webley, 2007; Zhang, Lv, et al., 2011). Closely packed $Bi_2Fe_4O_9$ nanowire arrays have been prepared via a citrate-based sol–gel method combined with a porous AAO template (Yang et al., 2006). In addition, $Bi_2Fe_4O_9$ nanoparticles have also been prepared by the polyacrylamide gel route, using various chelating agents (Zhang, Yang, et al., 2011). Park et al. (2005) fabricated submicron-sized $Bi_2Fe_4O_9$ cubes by employing the molten salt technique. However, both the sol–gel and molten salt methods require a high reaction temperature (>700 °C). The hydrothermal process is one of the most promising routes because of several advantages: mild environment, simply process, well-controlled morphology and low cost. Zhang et al. (2007) synthesized $Bi_2Fe_4O_9$ submicrocrystals with tunable morphologies,

* Corresponding author. Tel.: +86 551 2905285; fax: +86 551 2905285.
E-mail address: piezolab@hfut.edu.cn (R. Zuo).

1674-2001/$ – see front matter © 2012 Chinese Society of Particuology and Institute of Process Engineering, Chinese Academy of Sciences. Published by Elsevier B.V. All rights reserved.
http://dx.doi.org/10.1016/j.partic.2012.11.002

including sheets, plates, and cubes, by carefully adjusting the hydrothermal reaction conditions, and rod- and fiber-like morphologies were obtained in the presence of polyvinyl alcohol and at high concentrations of NaOH (12 M). Du et al. (2011) prepared microcylinders via the hydrothermal route by using the mineralizer NH_4OH. Wang et al. (2009) also reported that $Bi_2Fe_4O_9$ nanoparticles were synthesized at temperatures as low as 100 °C, via a hydrothermal method. These previous studies demonstrated that the morphology and the particle size of $Bi_2Fe_4O_9$ particles synthesized via a hydrothermal route were strongly dependent on the treatment conditions, additives, and solvents. Additionally, the magnetic and photocatalytic properties of $Bi_2Fe_4O_9$ crystals with different morphologies were also studied, demonstrating that the photocatalytic activity of the $Bi_2Fe_4O_9$ samples largely depended on the crystal morphology (Han, Huang, Jia, et al., 2006; Ruan & Zhang, 2009; Zhang, Lv, et al., 2011). It has been reported that by the introduction of inorganic salts into the hydrothermal process, the morphology and phase structure of prepared powders could be changed. Wang, Xu, Ren, et al. (2007) found that $BiFeO_3$ nanoparticles of 5 nm in diameter could be obtained in the presence of KNO_3, but the phase structure varied from $BiFeO_3$ to $Bi_{12}(Bi_{0.5}Fe_{0.5})O_{19.5}$ as $LiNO_3$ was gradually introduced (Wang, Xu, Yang, et al., 2007). Zhu et al. (2011) synthesized spherical $BiFeO_3$ nanocrystals in the presence of Na_2CO_3, while sillenite-type $Bi_{12}Fe_{0.63}O_{18.945}$ particles with hexagonal morphologies were obtained in the absence of Na_2CO_3. These previous works demonstrated that the use of inorganic salts in the hydrothermal process may contribute to the control of crystal morphology. Moreover, when compared with organic surfactants, inorganic salts were easily removed from the hydrothermal process by washing with distilled water.

The purpose of this study is to control the morphology of synthesized $Bi_2Fe_4O_9$ particles by introducing inorganic salt (KNO_3) during the hydrothermal process. Rectangular rod-like $Bi_2Fe_4O_9$ microcrystals were successfully obtained using a relatively low concentration of NaOH (5 M) and with the temperature maintained below 200 °C. The size of the obtained crystals was comparable to those previously synthesized by the molten salt technique. Moreover, a possible formation mechanism for the $Bi_2Fe_4O_9$ microrods was proposed by means of a series of time-dependent hydrothermal tests.

2. Experimental

2.1. Synthesis

All reagents were of analytical grade and were used without further purification. First, 2.0 mmol $Bi(NO_3)_3{\cdot}5H_2O$ and 4.0 mmol $Fe(NO_3)_3{\cdot}9H_2O$ were dissolved in 10 mL diluted HNO_3 (2 M) to form aqueous solutions. Glycerol was then introduced into the Bi–Fe solution while stirring at a temperature of 80 °C. During the process, the molar ratio of metal ions to hydroxyl groups in glycerol (M/–OH) was 1:1.5. With the evaporation of superfluous water under continuous heating at 80 °C and constant stirring, the volume of the solution decreased and the solution viscosity progressively increased. A brown solution was formed, accompanied by the volatilization of NO_x gas, which resulted from the decomposition of nitrate ions. A certain amount of NaOH solution, which served as a mineralizer, was added to the solution. The molar concentration of the mineralizer for the hydrothermal synthesis was 5 M. After stirring for 30 min, the reaction mixture was transferred to a Teflon-lined stainless steel autoclave and heated at 200 °C under auto-generated pressure for 24 h. After the end of the reaction, the autoclave was allowed to naturally cool to room temperature. The products were collected via centrifugation and then washed with water and ethanol several times. Finally, the samples were dried at 70 °C for 6 h. The mineralizer-assisted hydrothermal process was conducted by repeating the above procedure and adding 0.2 mol KNO_3 to the autoclave as a mineralizer.

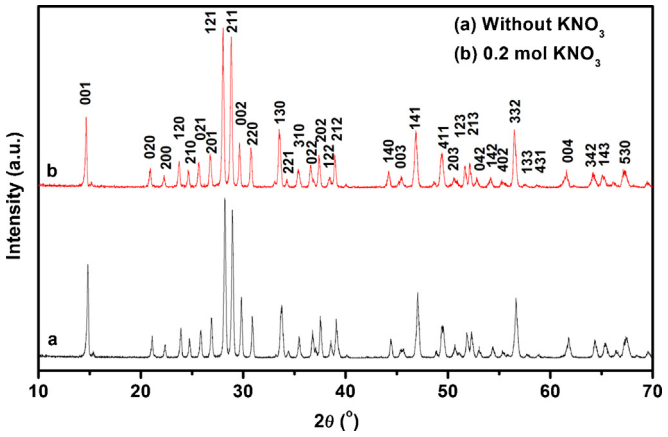

Fig. 1. XRD patterns of the as-prepared powders synthesized by the hydrothermal reaction at 200 °C for 24 h (a) in the absence of KNO_3 and (b) in the presence of 0.2 mol KNO_3.

2.2. Characterization

The products were analyzed by an X-ray diffractometer (XRD, D/Max-RB, Rigaku, Japan) using a Cu Kα source in a 2θ range from 10 to 70°. The product morphology was investigated with a scanning electron microscope (SEM, SSX-550, Shimadzu, Japan) and a transmission electron microscope (TEM, JEM-2010, JEOL, Japan, operated at an accelerating voltage of 200 kV). UV–vis diffuse reflectance spectra (DRS) of the samples were measured using barium sulfate as a standard, by a UV–vis spectrophotometer (TU-1950, Beijing Perkinje General Instrument Co., Ltd., Beijing, China) with an integrating sphere. The photocatalytic activity of the $Bi_2Fe_4O_9$ samples was evaluated under irradiation by a 400 W metal-halide lamp ($\lambda > 410$ nm) at its natural pH value. The initial concentration of methyl orange (MO) was 20 mg/L, with a catalyst loading of 0.5 g/L. Before illumination, the solution was stirred for 30 min in the dark to reach the adsorption–desorption equilibrium between the photocatalyst and MO. After 1 h, a small quantity of the solution was sampled, and the concentration of MO was determined by measuring the absorbance at approximately 464 nm using an UV–vis spectrophotometer. Each time before the absorption measurement, the sample solution was centrifuged for 30 min to separate the catalyst powder from the solution. The absorption was converted to the MO concentration and referenced against a standard curve to demonstrate a linear behavior between the concentration and the absorption at this wavelength.

3. Results and discussion

3.1. Crystallographic analysis

The XRD patterns of the products synthesized under different hydrothermal conditions are shown in Fig. 1. Pattern (a) shows the XRD pattern of the as-prepared samples prepared in the absence of KNO_3. It is evident that the diffraction peaks of the pattern (a) are well assigned to a pure-phase $Bi_2Fe_4O_9$ (JCPDS No. 25-0090, space group: Pbam) with the lattice parameters $a = 7.977$ Å, $b = 8.450$ Å, and $c = 6.007$ Å. No other peaks were observed. In addition, the sharp diffraction peaks demonstrate that well-crystallized $Bi_2Fe_4O_9$ can be obtained under the described hydrothermal

conditions. Pattern (b) displays the XRD pattern of the products synthesized in the presence of KNO_3 as the mineralizer. The diffraction pattern (b) shows a high level of crystallinity and is also indexed to a pure-phase $Bi_2Fe_4O_9$. No significant differences were observed between patterns (a) and (b). The results indicate that the use of KNO_3 mineralizer does not make a difference in the phase structure of the as-prepared $Bi_2Fe_4O_9$ particles.

3.2. Morphological analysis

The particle morphology of $Bi_2Fe_4O_9$ synthesized under different hydrothermal conditions is shown in Fig. 2. It can be seen from Fig. 2(a) that the as-synthesized $Bi_2Fe_4O_9$ crystals are primarily composed of a large quantity of submicron-sized particles with an average particle size of 300–500 nm, as the KNO_3 mineralizer was not used. The TEM image of the product (Fig. 2(b)) also shows submicron-sized particles with irregular morphologies, which confirms the particle size distribution that was estimated from the SEM images. In addition, the as-synthesized particles are well dispersed, and no obvious particle agglomeration is observed. However, in the presence of the KNO_3 mineralizer, the dominant products consisted of rectangular rod-like $Bi_2Fe_4O_9$ microcrystals with a large longitudinal dimension, as shown in Fig. 2(c). Most of these microcrystals have a length of 4 μm, a thickness of 200 nm and widths ranging from 150 to 800 nm. It is evident that the KNO_3 mineralizer plays a significant role in controlling the shape of the as-prepared $Bi_2Fe_4O_9$.

The morphology and fine structure of the rod-like products were further examined by TEM. As depicted in Fig. 3(a), the products have well-defined rod-like shapes with smooth surfaces, but have a heterogeneous size distribution, which is in good agreement with the SEM observations. It is of interest to note that some inclined faces were clearly observed at the ends of the rod-like crystals. The reason for the appearance of the inclined faces will be mentioned later. Fig. 3(b) shows a high-resolution TEM image that exhibits a continuous lattice strip. Fast Fourier transform (FFT) analysis is displayed in the inset of Fig. 3(b). The single-crystal nature of the material can be confirmed from the high-resolution TEM image. Interplanar spacings of 0.594 nm and 0.585 nm were calculated corresponding to the (0 0 1) and (1 1 0) planes of the orthorhombic $Bi_2Fe_4O_9$, respectively. These results imply that the rod-like crystals grow preferentially along the [0 0 1] direction.

3.3. Formation mechanism of the rod-like $Bi_2Fe_4O_9$ crystals

Fig. 4 demonstrates the influence of the KNO_3 mineralizer concentration on the morphology of hydrothermally synthesized

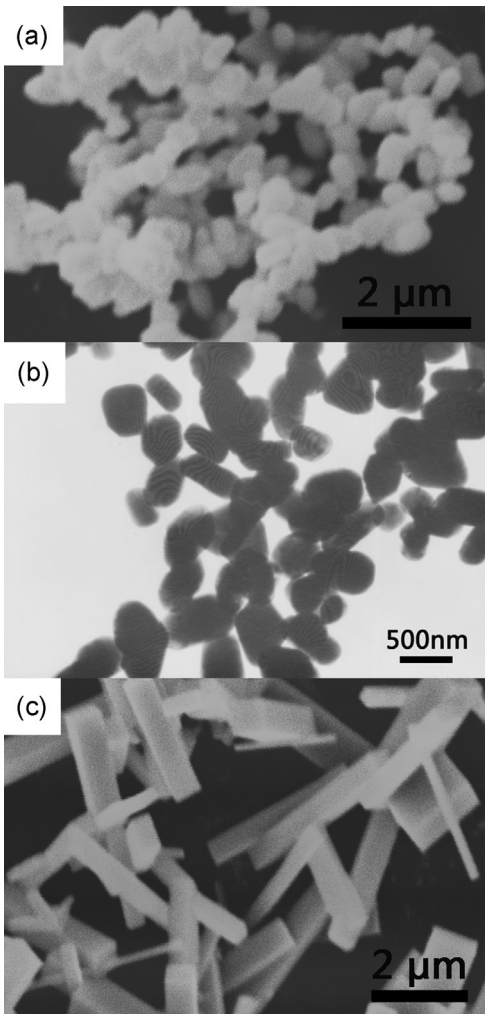

Fig. 2. (a) SEM and (b) TEM images of the as-prepared samples synthesized without KNO_3, and (c) SEM image of the samples synthesized with 0.2 mol KNO_3.

$Bi_2Fe_4O_9$ powders. The SEM images of the $Bi_2Fe_4O_9$ crystals synthesized with the addition of 0.1 and 0.3 mol KNO_3 are shown in Figs. 4(a) and (b), respectively. Coexisting particles in the shapes of cubes and short rods were observed when 0.1 mol KNO_3 was added, as can be seen in Fig. 4(a). Only larger rod-like crystals were obtained when the amount of KNO_3 was increased to 0.2 mol (Fig. 2(c)). As the amount of KNO_3 was further increased to 0.3 mol,

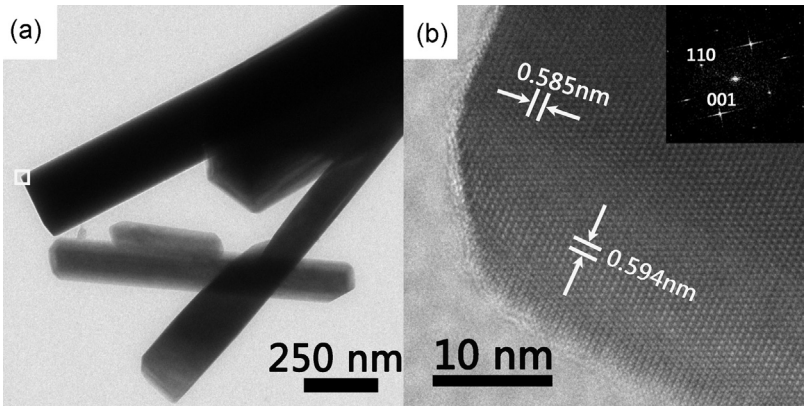

Fig. 3. (a) TEM and (b) HRTEM images of the as-prepared samples synthesized with 0.2 mol KNO_3. The inset in (b) shows the corresponding FFT pattern.

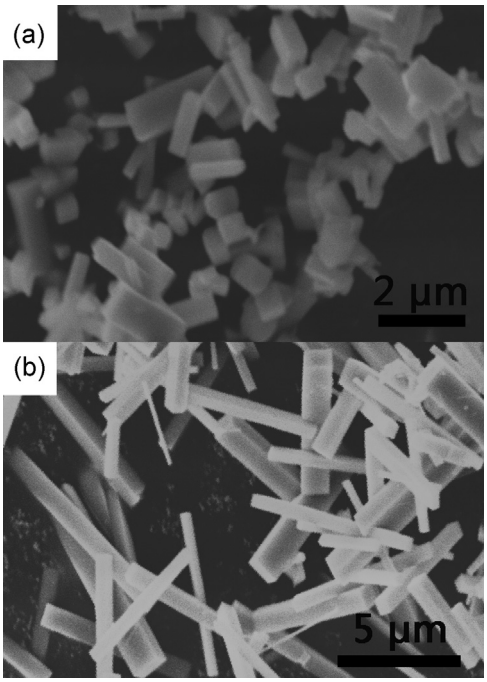

Fig. 4. SEM images of the as-prepared samples synthesized in the presence of (a) 0.1 mol and (b) 0.3 mol KNO_3.

the as-prepared product consisted only of even larger rod-like particles (~7 μm in length), as shown in Fig. 4(b). In addition, to investigate the morphological evolution of $Bi_2Fe_4O_9$ particles under the addition of 0.2 mol KNO_3, a series of experiments with different reaction times were conducted, with each set corresponding to a different stage of the hydrothermal reaction. Fig. 5 shows the SEM morphology of the products at each stage. After hydrothermal treatment for 3 h, the products were composed of irregular aggregates and rod-like particles (Fig. 5(a)). By further increasing the reaction time to 6 h, the aggregates were observed to disappear and most of the products appeared as rod-like crystals, on which some nanoparticles were observed (Fig. 5(b)). When the reaction time was prolonged to 10 h, the products consisted of larger rod-like particles with smooth surfaces (Fig. 5(c)). It has been reported that the use of different alkali metal ions in the hydrothermal synthesis of $BiFeO_3$ particles could result in the formation of different morphologies and crystal structures (Hojamberdiev et al., 2009; Wang, Xu, Yang, et al., 2007). Therefore, to clarify whether K^+ plays an important role in changing the $Bi_2Fe_4O_9$ crystal morphology, a contrast experiment was conducted, in which KNO_3 was replaced by equimolar amounts of $NaNO_3$, and other reaction conditions were kept unchanged. It can be seen that the substitution of 0.2 mol $NaNO_3$ for KNO_3 resulted in products with the same morphology, as shown in Fig. 6. This result demonstrated that K^+ is not the determining factor for the change in crystal growth behavior. Based on the time-dependent experiments, it was suggested that $Bi_2Fe_4O_9$ nanoparticles dissolve in the solution and grow on the surfaces of larger $Bi_2Fe_4O_9$ crystals, in a process known as Ostwald ripening. As previously reported, the dominant facets of the $Bi_2Fe_4O_9$ crystals are (0 0 1), (1 1 0) and ($\bar{1}$ 1 0) (Niizeki & Wachi, 1968). The morphology of the $Bi_2Fe_4O_9$ crystals can be described as a rectangular prism with (0 0 1), (1 1 0) and ($\bar{1}$ 1 0) planes. The schematic figure in Fig. 7 demonstrates that the crystal structure of $Bi_2Fe_4O_9$ consists of columns of the edge-sharing Fe–O octahedrons, which are corner-shared with corner-sharing Fe–O tetrahedrons. The Bi^{3+} ions are located in the spaces between the Fe–O polyhedrons. The Fe–O octahedrons, which are located on the layers perpendicular to

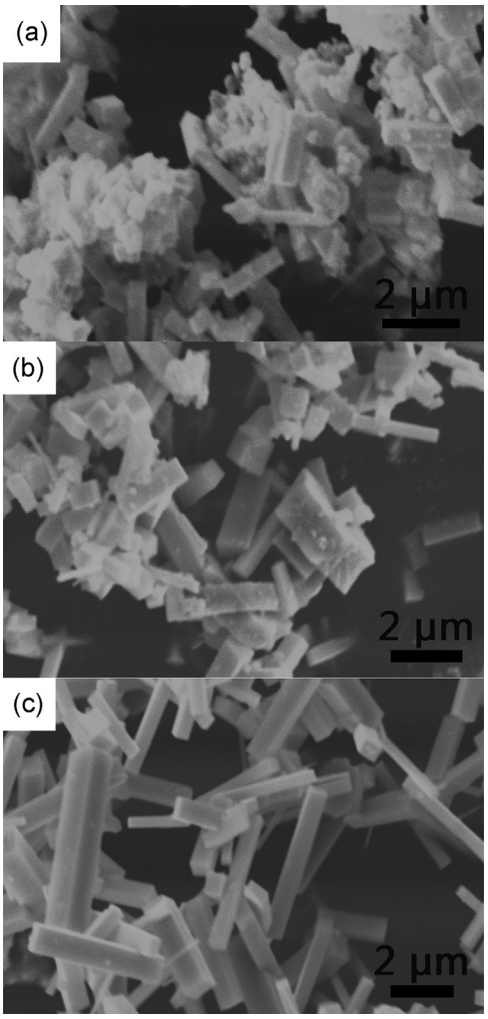

Fig. 5. SEM images of the $Bi_2Fe_4O_9$ samples synthesized in the presence of 0.2 mol KNO_3 following (a) 3 h-, (b) 6 h-, and (c) 10 h-hydrothermal treatment.

the c axis, are connected across the tetrahedron and bismuth oxide layer via edge-sharing oxygen that are located on the tetrahedron and bismuth oxide plane, respectively. The tetrahedrons, which are corner-shared along the (1 1 0) or ($\bar{1}$ 1 0) facets, are coupled perpendicular to the octahedron chains, thereby linking the chains to each other. The arrangement of the polyhedron indicates that the (0 0 1) facet is the most stable facet in the crystal (i.e. the surface energy of the (0 0 1) facet is lower than those of the (1 1 0) and ($\bar{1}$ 1 0) facets). During the initial stage of the hydrothermal process, a large

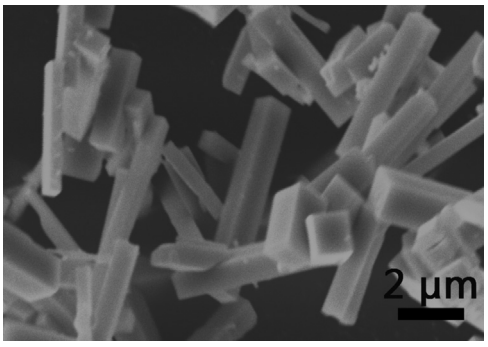

Fig. 6. SEM images of the as-prepared $Bi_2Fe_4O_9$ samples synthesized in the presence of 0.2 mol $NaNO_3$.

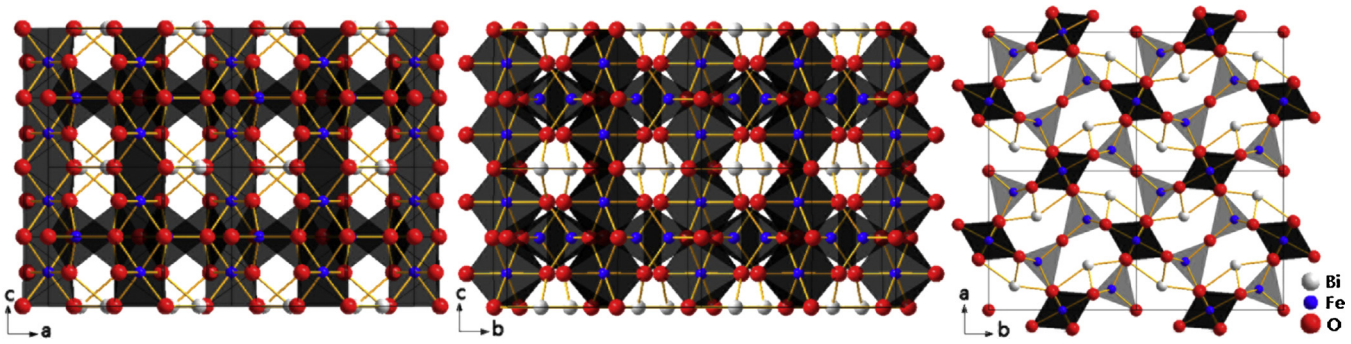

Fig. 7. Schematic illustration of the $Bi_2Fe_4O_9$ crystal structure viewed along different directions ($2 \times 2 \times 2$ cells).

number of small $Bi_2Fe_4O_9$ crystallites nucleate and grow into cubic-shape nanocrystals. It is well known that preferential anisotropic growth can be achieved by using surfactants (Peng & Manna, 2000), which permit selective adsorption onto certain faces of the crystals by means of hydrogen bonding or hydrophobic interactions in the hydrothermal environment (Paik, Hackley, & Lee, 1999). It is also believed that OH^- ions can behave as surfactants in the hydrothermal process (Han, Huang, Wu, et al., 2006; Zhang et al., 2007). In recent papers, Liu, Wu, Yin, Zhu, and Wang (2012) suggested that Al^{3+} ions can be adsorbed on the (1 1 0) or ($\bar{1}$ 1 0) facets, thereby serving as capping agents. It is presumed that NO_3^- promotes similar effects to those of OH^- and Al^{3+}. Because the surface energy of the (0 0 1) plane is much lower than those of the (1 1 0) and ($\bar{1}$ 1 0) planes, NO_3^- ions should preferentially be adsorbed on the (1 1 0) and ($\bar{1}$ 1 0) facets of the $Bi_2Fe_4O_9$ nanoparticles, thereby minimizing the surface energy through the formation of a protective layer. Due to the "blocking effect" of the NO_3^- ions, the growth rate on the (0 0 1) facet is higher than those on the (1 1 0) and ($\bar{1}$ 1 0) planes, thus inducing preferential growth along [0 0 1] direction. In addition, the formation of the inclined faces observed in the TEM image (Fig. 3) can also be attributed to the difference in growth rates on different crystal facets. The morphology evolution process of the rod-like $Bi_2Fe_4O_9$ crystals is illustrated in Fig. 8. The contribution of NO_3^- ions is also depicted in Figs. 2(c) and 4, in which the length of $Bi_2Fe_4O_9$ microrods increases with the concentration of NO_3^- ions in the reaction medium.

3.4. UV–vis analysis and photocatalytic performance

It is well known that UV–vis absorption is related to the electronic structure and the energy bands of the semiconductor catalyst. The absorption spectra of the as-prepared $Bi_2Fe_4O_9$ samples, both in the presence and absence of 0.2 mol KNO_3, are presented in Fig. 9(a). The spectra were transformed from the corresponding diffuse spectra according to Kubelka–Munk (K–M) theory (Kubelka & Munk, 1931). Two absorption bands are observed in the visible region, indicating that the sample can serve as a photocatalyst driven by visible light. The first absorption from 410 to 610 nm primarily results from two types of excitations overlapping each other. The first excitation process is due to the pair excitation processes: $^6A_{1g} + {}^6A_{1g} \rightarrow {}^4T_{1g}(^4G) + {}^4T_{1g}(^4G)$, and the second one is due to the excitation from $^6A_{1g}$ to ^4Eg, $^4A_{1g}(^4G)$ ligand field transitions (octahedral coordination) and $^6A_1$ to $^4T_2(^4G)$ ligand field transitions (tetrahedral coordination) as well as the charge-transfer band tail. The second absorption from 610 to 770 nm can then be assigned to the d–d transitions of Fe^{3+} (He et al., 2005; Sherman, 1985). The energy bandgaps of the $Bi_2Fe_4O_9$ samples can be calculated from the tangent lines in the plot of the square root

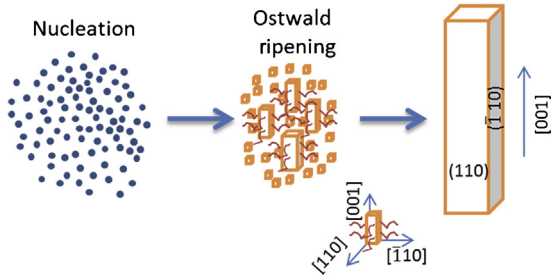

Fig. 8. Schematic illustration of the formation of rod-like $Bi_2Fe_4O_9$ microcrystals during the hydrothermal process.

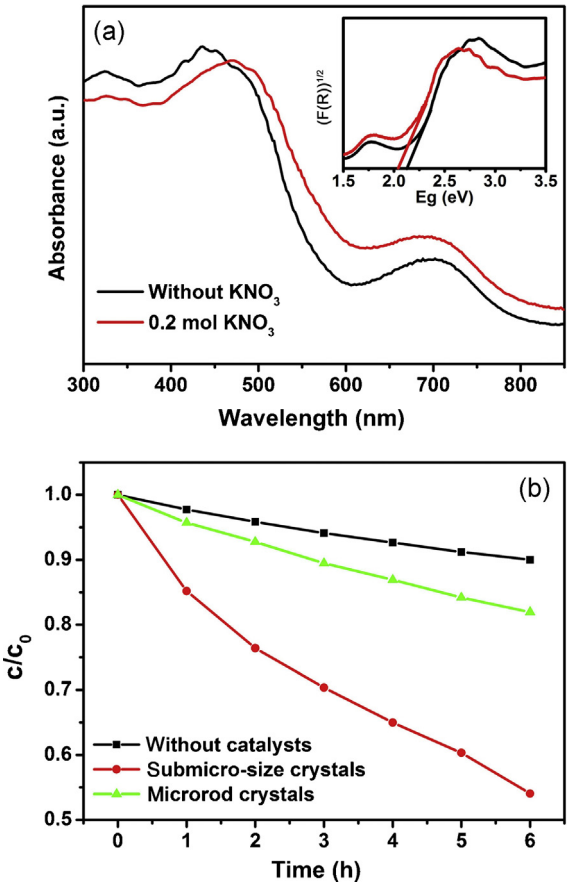

Fig. 9. (a) UV–vis absorption spectra of as-synthesized samples prepared without or with 0.2 mol KNO_3 and (b) photocatalysis of $Bi_2Fe_4O_9$ submicron-sized particles and microrods on the degradation of MO under visible light. The inset in (a) shows the square root of the Kubelka–Munk (K–M) function F(R) versus photon energy.

of K–M functions $F(R)$ against the photon energy (Kim, Atherton, Brigham, & Mallouk, 1993), as shown in the inset of Fig. 9(a). As the tangent lines are extrapolated to $(F(R))^{1/2} = 0$, the bandgaps of the submicron-sized $Bi_2Fe_4O_9$ particles and microrods were calculated to be 2.05 and 2.13 eV, respectively, which are comparable to the values previously reported (Sun et al., 2009). The visible-light photocatalytic activity of the $Bi_2Fe_4O_9$ samples was evaluated by using them to degrade the MO solution. Fig. 9(b) shows the photodegradation efficiency of the MO solution for submicron-sized $Bi_2Fe_4O_9$ particles and microrods under visible-light irradiation. Using the submicron-sized $Bi_2Fe_4O_9$ particles as photocatalyst, up to 45% MO was decolorized under visible-light illumination after 6 h. In contrast, less than 10% MO was degraded by the rod-like powders under the same experimental conditions. The differences in the photodegradation performances may be relevant to the particle sizes. It is known that when a photocatalytic reaction occurs at the interface between a catalyst and reagent, only the electron-hole pairs on the catalyst surface can participate in the photocatalytic reaction (Hoffmann, Martin, Choi, & Bahnemann, 1995; Ruan & Zhang, 2009). The electron-hole pairs require more time to diffuse to the surfaces of the sample when larger particle sizes are used. Therefore, the electron-hole recombination is more likely to occur in micron-sized rod-like $Bi_2Fe_4O_9$ samples than in submicron-sized $Bi_2Fe_4O_9$ samples during electron-hole diffusion. As a result, the photocatalytic activity of the microrods was lower. Moreover, the surface area of a catalyst plays a significant role in determining its catalytic potential. Generally, the surface area decreases as the particle size increases. Due to a decrease in particle size, the surface area of the submicron-sized $Bi_2Fe_4O_9$ crystals was significantly larger than that of the microrod-like crystals, which may also help to explain why the submicron-sized $Bi_2Fe_4O_9$ particles were capable of increased photocatalytic activity.

4. Conclusions

In the present study, the hydrothermal method was used to synthesize submicron-sized and micron-sized rod-like $Bi_2Fe_4O_9$ crystals in the absence and presence, respectively, of KNO_3. TEM analysis indicates that the synthesized $Bi_2Fe_4O_9$ microrods are present in a single-crystal structure and grow along the [0 0 1] direction. The morphology evolution of the $Bi_2Fe_4O_9$ microrods was investigated by varying the concentration of KNO_3 as well as the reaction time. The formation of rod-like $Bi_2Fe_4O_9$ crystals under hydrothermal conditions can be explained by the Ostwald ripening mechanism, combined with the hindrance effect of NO_3^- ions. Additionally, the optical absorption and photocatalytic activity of the as-synthesized $Bi_2Fe_4O_9$ samples were measured, thereby demonstrating the potential of $Bi_2Fe_4O_9$ as a visible light-driven photocatalyst.

Acknowledgments

This work was financially supported by funding from the Natural Science Foundation of Anhui Province (1108085J14) and the National Natural Science Foundation of China (50972035 and 51272060).

References

Du, Y., Cheng, Z., Dou, S., & Wang, X. (2011). Tunable morphology and magnetic properties of $Bi_2Fe_4O_9$ nanocrystal synthesized by hydrothermal method. *Journal of Nanoscience and Nanotechnology*, *11*, 2691–2695.

Fei, L. F., Yuan, J. K., Hu, Y. M., Wu, C. Z., Wang, J. L., & Wang, Y. (2011). Visible light responsive perovskite $BiFeO_3$ pills and rods with dominant $\{1\,1\,1\}_C$ facets. *Crystal Growth and Design*, *11*, 1049–1053.

Han, J. T., Huang, Y. H., Jia, R. J., Shan, G. C., Guo, R. Q., & Huang, W. (2006). Synthesis and magnetic property of submicron $Bi_2Fe_4O_9$. *Journal of Crystal Growth*, *294*, 469–473.

Han, J. T., Huang, Y. H., Wu, X. J., Wu, C. L., Wei, W., Peng, B., et al. (2006). Tunable synthesis of bismuth ferrites with various morphologies. *Advanced Materials*, *18*, 2145–2148.

He, Y. P., Miao, Y. M., Li, C. R., Wang, S. Q., Cao, L., Xie, S. S., et al. (2005). Size and structure effect on optical transitions of iron oxide nanocrystals. *Physical Review B*, *71*, 125411.

Hoffmann, M. R., Martin, S. T., Choi, W. Y., & Bahnemann, D. W. (1995). Environmental applications of semiconductor photocatalysis. *Chemical Reviews*, *95*, 69–96.

Hojamberdiev, M., Xu, Y. H., Wang, F. Z., Wang, J., Liu, W. G., & Wang, M. Q. (2009). Morphology-controlled hydrothermal synthesis of bismuth ferrite using various alkaline mineralizers. *Ceramics-Silikaty*, *53*, 113–117.

Kim, Y. I., Atherton, S. J., Brigham, E. S., & Mallouk, T. E. (1993). Sensitized layered metal oxide semiconductor particles for photochemical hydrogen evolution from nonsacrificial electron donors. *The Journal of Physical Chemistry*, *97*, 11802–11810.

Kubelka, P., & Munk, F. (1931). Ein beitrag zur optik der farbanstriche. *Zeitschrift für Technische Physik*, *12*, 593–601.

Li, S., Lin, Y. H., Zhang, B. P., Wang, Y., & Nan, C. W. (2010). Controlled fabrication of $BiFeO_3$ uniform microcrystals and their magnetic and photocatalytic behaviors. *The Journal of Physical Chemistry C*, *114*, 2903–2908.

Liu, Z. S., Wu, B. T., Yin, D. G., Zhu, Y. B., & Wang, L. G. (2012). Enhanced photocatalytic activity in Al-substituted $Bi_2Fe_4O_9$ submicrocrystals. *Journal of Materials Science*, *47*, 6777–6783.

Niizeki, N., & Wachi, M. (1968). The crystal structures of $Bi_2Mn_4O_{10}$, $Bi_2Al_4O_9$ and $Bi_2Fe_4O_9$. *Zeitschrift für Kristallographie*, *127*, 173–187.

Paik, U., Hackley, V. A., & Lee, H.-W. (1999). Dispersant-binder interactions in aqueous silicon nitride suspensions. *Journal of the American Ceramic Society*, *82*, 833–840.

Park, T. J., Papaefthymiou, G. C., Moodenbaugh, A. R., Mao, Y., & Wong, S. S. (2005). Synthesis and characterization of submicron single-crystalline $Bi_2Fe_4O_9$ cubes. *Journal of Materials Chemistry*, *15*, 2099–2105.

Peng, X. G., & Manna, L. (2000). Shape control of CdSe nanocrystals. *Nature*, *404*, 59–61.

Poghossian, A. S., Abovian, H. V., Avakian, P. B., Mkrtchian, S. H., & Haroutunian, V. M. (1991). Bismuth ferrites: New materials for semiconductor gas sensors. *Sensors and Actuators B: Chemical*, *4*, 545–549.

Ruan, Q. J., & Zhang, W. D. (2009). Tunable morphology of $Bi_2Fe_4O_9$ crystals for photocatalytic oxidation. *The Journal of Physical Chemistry C*, *113*, 4168–4173.

Sherman, D. M. (1985). The electronic structures of Fe^{3+} coordination sites in iron oxides: Applications to spectra, bonding, and magnetism. *Physics and Chemistry of Minerals*, *12*, 161–175.

Singh, A. K., Kaushik, S. D., Kumar, B., Mishra, P. K., Venimadhav, A., Siruguri, V., et al. (2008). Substantial magnetoelectric coupling near room temperature in $Bi_2Fe_4O_9$. *Applied Physics Letters*, *92*, 132910.

Sun, S. M., Wang, W. Z., Zhang, L., & Shang, M. (2009). Visible light-induced photocatalytic oxidation of phenol and aqueous ammonia in flowerlike $Bi_2Fe_4O_9$ suspensions. *The Journal of Physical Chemistry C*, *113*, 12826–12831.

Valant, M., & Suvorov, D. (2002). A stoichiometric model for sillenites. *Chemistry of Materials*, *14*, 3471–3476.

Voll, D., Beran, A., & Schneider, H. (2006). Variation of infrared absorption spectra in the system $Bi_2Al_{4-x}Fe_xO_9$ ($x = 0$–4), structurally related to mullite. *Physics and Chemistry of Minerals*, *33*, 623–628.

Wang, J., Neaton, J. B., Zheng, H., Nagarajan, V., Ogale, S. B., Liu, B., et al. (2003). Epitaxial $BiFeO_3$ multiferroic thin film heterostructures. *Science*, *299*, 1719–1722.

Wang, Y. B., Sun, H. J., Zhou, J., Bo, L., Zhang, C. Y., & Chen, W. (2010). Study of hydrothermal synthesis and properties of $Bi_2Fe_4O_9$. *Functional Materials Letters*, *3*, 173–176.

Wang, Y. G., Xu, G., Ren, Z. H., Wei, X., Weng, W. J., Du, P. Y., et al. (2007). Mineralizer-assisted hydrothermal synthesis and characterization of $BiFeO_3$ nanoparticles. *Journal of the American Ceramic Society*, *90*, 2615–2617.

Wang, Y. G., Xu, G., Yang, L. L., Ren, Z. H., Wei, X., Weng, W. J., et al. (2007). Alkali metal ions-assisted controllable synthesis of bismuth ferrites by a hydrothermal method. *Journal of the American Ceramic Society*, *90*, 3673–3675.

Wang, Y. G., Xu, G., Yang, L. L., Ren, Z. H., Wei, X., Weng, W. J., et al. (2009). Low-temperature synthesis of $Bi_2Fe_4O_9$ nanoparticles via a hydrothermal method. *Ceramics International*, *35*, 51–53.

Xiong, Y., Wu, M., Peng, Z., Jiang, N., & Chen, Q. (2004). Hydrothermal synthesis and characterization of $Bi_2Fe_4O_9$ nanoparticles. *Chemistry Letters*, *33*, 502–503.

Yang, Z., Huang, Y., Dong, B., Li, H. L., & Shi, S. Q. (2006). Densely packed single-crystal $Bi_2Fe_4O_9$ nanowires fabricated from a template-induced sol–gel route. *Journal of Solid State Chemistry*, *179*, 3324–3329.

Yang, H. G., Sun, C. H., Qiao, S. Z., Zou, J., Liu, G., Smith, S. C., et al. (2008). Anatase TiO_2 single crystals with a large percentage of reactive facets. *Nature*, *453*, 638–641.

Yu, Z. W., Miao, H. Y., & Tan, G. Q. (2008). $Bi_2Fe_4O_9$ nanoparticles: Preparation by hydrothermal method and characterization. *Chinese Journal of Inorganic Chemistry*, *24*, 483–486.

Zakharchenko, N. I. (2002). Catalytic properties of the Fe_2O_3–Bi_2O_3 system in ammonia oxidation to nitrogen oxides. *Kinetics and Catalysis*, *43*, 95–98.

Zhang, X. Y., Bourgeois, L., Yao, J. F., Wang, H. T., & Webley, P. A. (2007). Tuning the morphology of bismuth ferrite nano- and microcrystals: From sheets to fibers. *Small*, *3*, 1523–1528.

Zhang, X. Y., Lv, J., Bourgeois, L., Cui, J., Wu, Y. C., Wang, H. T., et al. (2011). Formation and photocatalytic properties of bismuth ferrite sub-microcrystals with tunable morphologies. *New Journal of Chemistry*, *35*, 937–941.

Zhang, M., Yang, H., Xian, T., Wei, Z. Q., Jiang, J. L., Feng, Y. C., et al. (2011). Polyacrylamide gel synthesis and photocatalytic performance of $Bi_2Fe_4O_9$ nanoparticles. *Journal of Alloys and Compounds*, *509*, 809–812.

Zhu, X. H., Hang, Q. M., Xing, Z. B., Yang, Y., Zhu, J. M., Liu, Z. G., et al. (2011). Microwave hydrothermal synthesis, structural characterization, and visible-light photocatalytic activities of single-crystalline bismuth ferric nanocrystals. *Journal of the American Ceramic Society*, *94*, 2688–2693.